An anisotropic diffusion-based defect detection for sputtered surfaces with inhomogeneous textures

by

Du-Ming Tsai and Shin-Min Chao

Department of Industrial Engineering and Management
Yuan-Ze University, Taiwan, R.O.C.

Correspondence:

Du-Ming Tsai
Department of Industrial Engineering & Managment
Yuan-Ze University
135 Yuan-Tung Road
Nei-Li, Tao-Yuan
Taiwan, R.O.C.

Fax: +886-3- 4638907
E-Mail: iedmtsai@saturn.yzu.edu.tw

An anisotropic diffusion-based defect detection for sputtered surfaces with inhomogeneous textures

Abstract

Texture analysis techniques are being increasingly used for surface inspection, in which small defects that appear as local anomalies in textured surfaces must be detected. Traditional surface inspection methods mainly focus on homogeneous textures that contain periodical, repetitive patterns. In this paper, we study defect detection in sputtered glass substrates that involve inhomogeneous textures. Such sputtered surfaces can be found in touch panels and LCDs. An anisotropic diffusion scheme is proposed to detect subtle defects embedded in inhomogeneous textures. The proposed anisotropic diffusion model takes a nonnegative decreasing function with an annealing gradient threshold as the diffusion coefficient to adaptively adjust the significance of edge gradients. It triggers the smoothing process in faultless areas for background texture removal by assigning a large diffusion coefficient value, and stops the diffusion process in defective areas to preserve sharp edges of anomalies by assigning a small diffusion coefficient value. Experimental results from a number of sputtered glass samples have shown the effectiveness of the proposed anisotropic diffusion scheme.

Key words: Anisotropic diffusion; defect detection; inhomogeneous texture; sputtered surfaces

1. Introduction

Texture analysis techniques in image processing are being increasingly used to automate industrial inspection of material surfaces. In automatic surface inspection, one has to solve the problem of detecting small defects that appear as local anomalies in textured surfaces. In this paper, we focus on the problem of surface inspection in sputtered glass substrates that involve inhomogeneous textures. Such sputtered surfaces can be easily found in touch panels and liquid crystal displays. In sputtering processes, the coating must adhere well on the surface of the transparent glass or films and be free of contamination for the panels to perform to specification. Figure 1 presents two images of sputtered glass surfaces, of which Figure 1(a) is a faultless sputtered surface, and Figure 1(b) is a defective one. It can be seen from Figure 1(a) that the textured surface does not show the repetition, self-similarity property everywhere in the image.

The traditional texture analysis techniques for defect detection have been focused on homogeneously textured surfaces, in which repetitive, periodical patterns give harmonic visual impression in the whole image. Taking advantage of image homogeneity, those techniques generally compute a set of textural features in the spatial domain or in the spectral domain, and then search for significant local deviations in the feature values using various classifiers such as Bayes [1], maximum likelihood [2], Markov random field [3], and neural networks [4]. In spatial-domain approaches, the commonly used features are the second-order statistics derived from spatial gray-level co-occurrence matrices [5]. They have been successfully applied to wood inspection [6], carpet wear assessment [7], and roughness measurement of machined surfaces [8]. In spectral-domain approaches, textural features are generally derived from the Fourier transform [9, 10] for fabric defect detection [11, 12], patterned wafer inspection [13] and roughness classification of castings [14], the Gabor transform [15-17] for the inspection of wooden surfaces [18], granite [19], steel surfaces [20], textile fabrics [21], and homogeneously structural and statistical textures [22], and the wavelet transform [23, 24] for the inspection of industrial materials such as LSI wafers [25], woven fabrics [26], and textured surfaces [27].

Other than feature extraction methods, Tsai and Hsieh [28], and Tsai and Huang [29] proposed global approaches based on a 2D Fourier image reconstruction scheme for inspecting surface defects in structural and statistical textures. Their approaches first eliminated the frequency components that correspond to the homogeneous background texture using a bandreject technique, and then back-transformed the Fourier spectrum to a spatial-domain image. In this way, the periodical, repetitive texture patterns can be effectively removed, and only local anomalies will be preserved in the reconstructed image. Khalay [30] proposed a self-reference technique for detecting defects embedded in periodical structures that contain only horizontal and vertical line patterns. The repetitive periods of the pattern in both horizontal and vertical directions were evaluated by high-resolution spectral estimation techniques. Then a synthetic self-reference image was generated from the acquired image itself, and used for comparison with the actual image.

The local feature-extraction and global image-reconstruction approaches aforementioned are ideally suited for detecting local variations in homogeneous textures, and work successfully for a variety of material surfaces that contain periodical, repetitive patterns. However, they are not directly extensible to the inspection of sputtered glass substrates that involve inhomogeneous textures.

Observing from Figures 1(a) and (b), we find that the faultless sputtered surface presents the self-similarity of textured pattern in some regions, but not in the whole image. The irregular area in the faultless surface image cannot be distinctly discriminated from the anomalies in the defective surface image. This makes the detection of defects in inhomogeneous textures extremely difficult.

In this paper, we propose an anisotropic diffusion scheme to tackle the problem of defect inspection in sputtered glass substrates that contain inhomogeneous textures. Anisotropic diffusion was first proposed by Perona and Malik [31] for scale-space description of images and edge detection. This approach is basically a modification of the linear diffusion (or heat equation), and the continuous anisotropic diffusion is given by

$$\frac{\partial \boldsymbol{I}_t(x,y)}{\partial t} = \boldsymbol{div}\,[\boldsymbol{c}_t(x,y) \cdot \nabla \boldsymbol{I}_t(x,y)] \tag{1}$$

where $\boldsymbol{I}_t(x,y)$ is the image at time *t*, ***div*** the divergence operator, $\nabla \boldsymbol{I}_t(x,y)$ the gradient of the image, and $\boldsymbol{c}_t(x,y)$ the diffusion coefficient. If $\boldsymbol{c}_t(x,y)$ is a constant, equation (1) is then reduced to the isotropic diffusion equation, and is equivalent to convolving with a Gaussian. The idea of anisotropic diffusion is to adaptively choose $\boldsymbol{c}_t$ such that intra-regions become smooth while edges of inter-regions are preserved. The diffusion coefficient $\boldsymbol{c}_t$ is generally selected to be a nonnegative function of gradient magnitude so that small variations in intensity such as noise or shading can be well smoothed, and edges with large intensity transition are distinctly retained.

You *et al*. [32] gave an in-depth analysis of the behavior of the anisotropic diffusion model of Perona and Malik by considering the anisotropic diffusion as the steepest descent method for solving an energy minimization problem. Barash [33] addressed the fundamental relationship between anisotropic diffusion and adaptive smoothing. He showed that an iteration of adaptive smoothing

$$\boldsymbol{I}_{t+1}(x,y) = \frac{\sum_i \sum_j \boldsymbol{I}_t(x+i, y+j) w_t(x+i, y+j)}{\sum_i \sum_j w_t(x+i, y+j)} \tag{2}$$

is an implementation of the discrete version of the anisotropic diffusion equation if the weight w_t in eq. (2) is taken as the same of the diffusion coefficient $\boldsymbol{c}_t$. Weickert *et al*. [34] discussed that anisotropic diffusion filtering is performed with explicit schemes and tends to be computationally inefficient due to very small time steps. They presented a fast semi-implicit scheme, which is a Gaussian algorithm, for solving a tridiagonal system of linear equations. An increase of efficiency by a factor of 10 with the proposed scheme was reported in their experiments. The anisotropic diffusion approach has grown to become a useful tool for edge detection [35, 36], image enhancement [37, 38], image smoothing [39, 40], image segmentation [41, 42] and texture segmentation [43].

The problem of defect detection in sputtered glass substrates that contain inhomogeneous textures is different from the classical image segmentation that mainly involves multiple regions of uniform gray levels or multiple textures of homogeneous patterns in one image. In this paper, we use anisotropic diffusion to detect defects in sputtered glass surfaces that contain inhomogeneous textures. The anisotropic diffusion acts as a selective smoothing. It triggers the smoothing process in faultless areas for background texture removal, and stops the diffusion process in defective areas to preserve sharp edges of anomalies. Two diffusion coefficient functions with an adaptive-function parameter are evaluated for the specific application of sputtered glass inspection. The adaptive-function parameter will be annealed over time so that the diffusion process will effectively smooth irregular background textures, and yet distinctly preserve anomalies in the sputtered glass surfaces.

This paper is organized as follows. Section 2 first overviews the anisotropic diffusion equation of Perona and Malik, and then discusses the proposed anisotropic diffusion model that involves a nonlinear diffusion coefficient with annealing parameter. Section 3 presents the experimental results from a variety of sputtered glass surfaces that contain various defects. The effects of different anisotropic coefficient functions and annealing parameter functions are also analyzed. The paper is concluded in Section 4.

2. The anisotropic diffusion model for defect detection

Let $\boldsymbol{I}_t(x, y)$ be the gray level at coordinates (x, y) of a digital image at iteration t, and $\boldsymbol{I}_0(x, y)$ the original input image. The continuous anisotropic diffusion in eq. (1) can be discretely implemented using four nearest neighbors and the Laplacian operator [39]

$$\boldsymbol{I}_{t+1}(x, y) = \boldsymbol{I}_t(x, y) + \frac{1}{4}\sum_{i=1}^{4}[\boldsymbol{c}_t^i(x, y) \cdot \nabla \boldsymbol{I}_t^i(x, y)]$$

where $\nabla \boldsymbol{I}_t^i(x, y)$, i = 1, 2, 3 and 4, represent the gradients of four neighbors in the north, south, east and west directions, respectively, i.e

$$
\begin{aligned}
\nabla \boldsymbol{I}_t^1(x, y) &= \boldsymbol{I}_t(x, y-1) - \boldsymbol{I}_t(x, y) \\
\nabla \boldsymbol{I}_t^2(x, y) &= \boldsymbol{I}_t(x, y+1) - \boldsymbol{I}_t(x, y) \\
\nabla \boldsymbol{I}_t^3(x, y) &= \boldsymbol{I}_t(x+1, y) - \boldsymbol{I}_t(x, y) \\
\nabla \boldsymbol{I}_t^4(x, y) &= \boldsymbol{I}_t(x-1, y) - \boldsymbol{I}_t(x, y)
\end{aligned}
$$

$\boldsymbol{c}_t^i(x, y)$ is the diffusion coefficient associated with $\nabla \boldsymbol{I}_t^i(x, y)$, and can be considered as a function of the magnitude of gradient $\nabla \boldsymbol{I}_t^i(x, y)$, i.e,

$$\boldsymbol{c}_t^i(x, y) = g(\nabla \boldsymbol{I}_t^i(x, y))$$

For the sack of simplicity, $\nabla \boldsymbol{I}_t^i(x, y)$ is subsequently denoted by $\nabla \boldsymbol{I}$. $g(\nabla \boldsymbol{I})$ has to be a nonnegative monotonically decreasing function with $g(0) = 1$ and $\lim_{|\nabla I| \to \infty} g(\nabla \boldsymbol{I}) = 0$. The selection of $g(\nabla \boldsymbol{I})$ is to have a low coefficient value at image edges of anomalies, and a high coefficient value within image regions so that unwanted background textures are thoroughly smoothed and inter-region edges of defects are preserved. Two possible diffusion coefficient functions are

$$g(\nabla \boldsymbol{I}) = \exp[-(|\nabla \boldsymbol{I}| / \mathcal{K})^2] \tag{3}$$

and

$$g(\nabla \boldsymbol{I}) = 1 / [1 + (|\nabla \boldsymbol{I}| / \mathcal{K})^2] \tag{4}$$

In the anisotripic diffusion model of Perona and Malik [31], the parameter $\mathcal{K}$ is a constant, and must be fine-tuned for a particular application. Parameter $\mathcal{K}$ in the diffusion coefficient function acts as an edge strength threshold. If the $\mathcal{K}$ value is an overly small constant in all diffusion iterations, the diffusion will stop in early iterations and the background texture cannot be sufficiently smoothed. This may cause false rejection of a faultless surface in the inspection process. Reversely, if the $\mathcal{K}$ value is a large constant, the diffusion process will oversmooth in early iterations and both the background texture and defects will be removed. This may cause false acceptance of a defective surface accordingly.

Figures 2(a) and (b) depict the diffusion coefficient functions of eqs. (3) and (4), respectively. Let $\phi(\nabla \boldsymbol{I})$ be a flux function defined by [32]

$$\phi(\nabla \boldsymbol{I}) = g(\nabla \boldsymbol{I}) \cdot \nabla \boldsymbol{I} \tag{5}$$

A large flux value indicates a strong effect on smoothness. Figures 3(a) and (b) give the graphs of the flux functions of the respective diffusion coefficient functions in eqs. (3) and (4). For a given $\mathcal{K}$ value, it can be seen from Figure 2 that the diffusion coefficient function of eq. (3) drops dramatically and approximates to zero when the gradient magnitude $|\nabla \boldsymbol{I}|$ is larger than $2\mathcal{K}$, i.e., the diffusion stops as soon as $|\nabla \boldsymbol{I}| > 2\mathcal{K}$. The maximum smoothness occurs at $|\nabla \boldsymbol{I}| = 0.75\mathcal{K}$ as shown in the corresponding flux function. The diffusion coefficient function of eq. (4), instead, decreases more gradually even when $|\nabla \boldsymbol{I}| > 2\mathcal{K}$. Its corresponding flux function shows that the maximum smoothness is at $|\nabla \boldsymbol{I}| = 1\mathcal{K}$. Compared to eq. (4), eq. (3) privileges high-contrast edges over low-contrast ones. In the application of defect detection in sputtered glass substrates, diffusion coefficient function of eq. (4) is more desirable than that of eq. (3).

The sputtered glass surfaces involve inhomogeneous textures in nature and some faultless regions may contain irregular items. The diffusion coefficient function of eq. (3) may cause the diffusion process to stop in the early iterations, and the background texture will not be sufficiently removed. Given that the gradient threshold $\mathcal{K}$ is a constant, the selection of a best $\mathcal{K}$ value becomes extremely crucial. A large $\mathcal{K}$ value will oversmooth both background textures and defects. An overly small $\mathcal{K}$ value disables the diffusion process and the unwanted background texture will be preserved.

In order to alleviate the limitations of the use of a constant $\mathcal{K}$, we propose an annealing *n*-th root function for the gradient threshold $\mathcal{K}$. Its value will be reduced as the diffusion iteration increases. In each diffusion iteration, the gradient magnitude (i.e. intensity contrast) of anomalies will be reduced in the filter image. A constant $\mathcal{K}$ will eventually smooth out the defects. However, as the gradient threshold adaptively decreases with the increment of iterations, the diffusion process has no effect on the defective regions while it can gradually remove the background textures as long as the decrement of gradient magnitude in faultless regions is competitive with the decrement of the $\mathcal{K}$ value. The annealing *n*-th root function used in this study is defined by

$$\mathcal{K}(t) = \mathcal{K}(0) \cdot t^{-\frac{1}{n}} \tag{6}$$

where $\mathcal{K}(t)$ is the gradient threshold at iteration t, $\mathcal{K}(0)$ is the initial value, and *n* is a positive integer. Figures 4(a)-(d) present the graphs of four root functions with *n* = 1, 2, 3 and 4, respectively. Note how the shape of the function is affected as the value of *n* is changed. The graphs show that a small *n*, such as *n* = 1, will make the $\mathcal{K}$ value drop rapidly and cause the diffusion process to stop at a small number of iterations t. As *n* increases, the $\mathcal{K}$ value will decrease gradually and result in fast smoothness in a small number of iterations. An overly large value of n may oversmooth both background textures and subtle defects in early iterations. Figure 5(a) shows a sputtered glass substrate containing defects on the surface, and Figures 5(b)-(e) present the diffusion results from the four root functions with n = 1, 2, 3 and 4 at the iteration numbers t = 50, 100 and 150. The results in Figures 5(b1)-(b3) reveal that the background texture cannot be effectively removed even after 150 iterations when the annealing root function is given by $\mathcal{K}(t) = \mathcal{K}(0) \cdot t^{-1}$ (i.e., n = 1). When the quadruple root function (i.e., n = 4) is used, the background texture is significantly smoothed at a small iteration number of 50, and some details of defects are blurred at a large iteration number of 150. Two additional sample images, one containing a black line defect, and the other containing a white scratch defect as shown in Figure 6, are used to further evaluate the diffusion effects of varying annealing root functions. The diffusion results consistently reveal that the annealing cubic-root function can effectively remove background textures and well preserve most of the defect regions. By considering the objective of background-texture removal and defect preservation in the filter image, the annealing cubic-root function

$$\mathcal{K}(t) = \mathcal{K}(0) \cdot t^{-\frac{1}{3}}$$

is adapted in this study for the application of defect detection in sputtered glass surfaces. The diffusion coefficient function used in this study is therefore given by

$$\boldsymbol{c}_t^i(x,y) = g(\nabla \boldsymbol{I}_t^i(x,y)) = \frac{1}{1 + [\left|\nabla \boldsymbol{I}_t^i(x,y)\right| \big/ \mathcal{K}(0) \cdot t^{-\frac{1}{3}}]^2} \tag{7}$$

Since the gradient threshold value $\mathcal{K}$ is adaptively decreased as the iteration number increases, the selection of the initial value $\mathcal{K}(0)$ is not as crucial as that of a constant $\mathcal{K}$ in the Perona and Malik's model. Given a sputtered surface image that contains anomalies, we can generally expect that the average gradient magnitude of the defective region is larger than that of the faultless region, and the average gradient magnitude of the whole image is somewhere in between. As seen in Figure 3(b), the flux function of the diffusion coefficient in eq. (4) shows that the maximum smoothness is given by $\left|\nabla \boldsymbol{I}\right| = 1 \cdot \mathcal{K}$. We therefore set the initial value $\mathcal{K}(0)$ of the annealing cubic root function to the average gradient magnitude of the whole image under inspection, i.e.,

$$\mathcal{K}(0) = \frac{1}{4M \cdot N} \sum_{i=1}^{4} \sum_{x=0}^{M-1} \sum_{y=0}^{N-1} \nabla \boldsymbol{I}_t^i(x, y)$$

where $M \cdot N$ is the image size. A thorough experiment from a variety of sputtered glass samples has shown that the selected $\mathcal{K}(0)$ works successfully for the defect detection application.

3. Experimental results

In this section, we present experimental results from a number of sputtered glass substrates involving various defects. The algorithms are implemented on a Pentinum 4, 1.9G personal computer using the VB language. The image is 200×200 pixels wide with 8-bit gray levels. Since the inspection task is a supervised one, the required minimum number of iterations t is selected in advance such that the background textures of faultless samples can be sufficiently removed. Computation time of the proposed anisotropic diffusion scheme is linearly proportional to the number of iterations. For instance, computation times of 30 and 100 iterations on a 200×200 image are 0.45 and 1.32 seconds, respectively.

As seen previously, Figures 1(a) and (b) show respectively a faultless sample and a defective sample of sputtered glass surfaces that contain irregular texture structures. The diffusion results of these two test samples from the diffusion coefficient functions of eqs. (3) and (4) with an annealing cubic-root function are demonstrated in Figures 7 and 8. The same initial gradient threshold $\mathcal{K}(0) = 5$ is applied to all experiments of the two test samples. For both the faultless and defective surface samples, the diffusion coefficient function of eq. (4) yields an approximately uniform image at iteration number 30, and makes the diffusion process steady after iteration number 50. However, the diffusion coefficient function of eq. (3) cannot sufficiently remove the background texture at iteration number 30, and some noisy blobs remain in the filter image even at the iteration number 100, as seen in Figures 7(b2)-(b4) and 8(b2)-7(b4).

To compare the diffusion effect between an annealing gradient threshold $\mathcal{K}(t)$ and a constant $\mathcal{K}$, Figures 9 and 10 further present the diffusion results on the two test samples in Figures 1(a) and (b) using a large constant $\mathcal{K} = 5$ (the initial value $\mathcal{K}(0)$ used in the cubic-root function), and a small constant $\mathcal{K} = 1$ in the diffusion coefficient function of eq. (4). It reveals that the large constant $\mathcal{K} = 5$ oversmoothes the texture surface, and the resulting defect in Figure 10(a1)-(a4) is severely blurred. The small constant $\mathcal{K} = 1$ has only small effect on diffusion, and the detailed background texture remains in the filter image even after 100 iterations, as seen in Figure 10(b1)-(b4).

In order to identify the defect regions in the final diffused image, the edges of anomalies are detected by comparing their gradient magnitude with respect to a specific threshold. Let t^* be the stopping iteration number of diffusion. $\boldsymbol{I}_{t^*}(x, y)$

is then the final diffused image. The gradient magnitude of a pixel at coordinates (x, y) is defined by the average of $\nabla \boldsymbol{I}_{t^*}^{i}(x, y)$, i = 1, 2, 3, 4, i.e.,

$$\nabla \bar{\boldsymbol{I}}_{t^*}(x, y) = \frac{1}{4}\sum_{i=1}^{4} \nabla \boldsymbol{I}_{t^*}^{i}(x, y)$$

In the proposed anisotropic diffusion model, the edge gradient $\nabla \boldsymbol{I}$ is compared with the edge strength threshold $\mathcal{K}(t)$. Therefore, we simply use $\mathcal{K}(t^*)$ as the gradient threshold, where

$$\mathcal{K}(t^*) = \mathcal{K}(0) \cdot (t^*)^{-\frac{1}{3}}$$

When the gradient $\nabla \bar{\boldsymbol{I}}_{t^*}(x, y)$ of a pixel at (x, y) is larger than the threshold $\mathcal{K}(t^*)$, pixel (x, y) is classified as an edge point. Otherwise, it is a within-region pixel. A long edge segment indicates the evidence of a defect in the sputtered surface. The sample images in Figures 1(a) and (b) are again employed to demonstrate the edge detection and thresholding results of defect regions in the final diffused image. Figures 11(a2) and (b2) show the resulting diffusion images at iteration number 150, both with $\mathcal{K}(0) = 5$. Figures 11(a3) and (b3) present the detected edges of defect regions as binary images. Note that Figure 11(a3) contain no edges, except for some minor noisy points, for the faultless sputtered surface, and Figure 11(b3) involves sizable connected edges of the defect regions for the defective sputtered surface. Figures 11(a4) and (b4) further illustrate the results of superimposing the detected edges in Figures 11(a3) and (b3) on the original images. The results reveal that the edges of defect regions are well detected and located.

Figures 12 further present eight additional test samples of sputtered glass surfaces under higher image resolution. The test images in Figures 12(b1)-(h1) show a variety of subtle defects. Some of them are very narrow in width, and do not show high-contrast intensities. The detection results at iteration number 50 with $\mathcal{K}(0) = 4$ for all eight test samples show that the proposed anisotropic diffusion scheme performs effectively to detect defects in the sputtered glass substrates that contain inhomogeneous textures. The detected edges of defect regions for the eight test samples are also illustrated in Figures 12(a3)-(h3). They are superimposed on the original images to show the effectiveness of detection and localization.

In order to verify the necessity of the proposed diffusion process for defect detection, Figures 13 and 14 present two pairs of test images used for the comparisons among the proposed diffusion method, and two simple smoothing methods of Gaussian filtering and median filtering. Both smoothing filters are of the size 3×3, and the filtering processes are iteratively repeated for 20 times so that the inhomogeneous background can be smoothed. The same edge detection method is applied in the filtered images for all three methods. The gradient threshold selected for each method has such a value that most of the true defects' edges can be effectively identified in the filtered images.

Each pair of the test images in Figure 13 or 14 involves a clear surface and a defective one. The detection results from the three methods are represented by superimposing the thresholded edges in the filtered images. The resulting images in Figures 13 and 14 show that the median filtering performs poorly, and the Gaussian filtering yields numerous noisy points in both faultless and defective sputtered surfaces. In contrast, the detection results from the proposed diffusion method are relatively clear for the faultless surface, while the anomalies are well detected for the defective surfaces. Therefore, the proposed diffusion process is mandatory for effective detection of defects in inhomogeneous sputtered surfaces.

4. Conclusions

In this paper we have proposed an anisotropic diffusion scheme for detecting defects in sputtered glass surfaces that involve inhomogeneous textures. Since a sputtered surface may involve irregularity in faultless areas, it makes the defect detection task extremely difficult. The diffusion coefficient of the anisotropic diffusion model used in this study is a nonnegative decreasing function, in which the gradient threshold $\mathcal{K}$ is chosen to be an annealing cubic-root function. The value of $\mathcal{K}$ can then adaptively determine the significance of the local gradient as the intensity-contrast in the filter image is gradually reduced in increasing number of iterations.

Experimental results have shown that the proposed anisotropic diffusion scheme can effectively remove background textures in faultless areas, and yet maintain sharp edges of anomalies in the filter image of a sputtered glass surface. The inherent limitation of the anisotropic diffusion model is that the convergence of the diffusion process is time-consuming. An efficient and fast computation version of anisotropic diffusion is worth further investigation so that defect detection in sputtered glass surfaces can be on-line applied in manufacturing.

The proposed method is directly related to nonlinear edge preserving smoothing techniques. The median filter is a simple non-linear filter that has been used extensively in edge-preserving smoothing. It does not provide sufficient smoothing with sharp-edge preservation, especially when the data is Gaussian in nature [44]. Markov random field (MRF) based methods [45, 46, 47] have achieved good segmentation results on a variety of images. The MRF-based methods generally transform image segmentation problem into an optimization problem. They require fairly accurate knowledge of the prior true image distribution, and most of them are quite computationally expensive for the parameter estimation [48]. The proposed anisotropic diffusion scheme for defect detection requires only the selection of the initial value of the gradient threshold; i.e., $\mathcal{K}(0)$, in the anisotropic diffusion model. It will then automatically and effectively smooth out the background texture and distinctly preserve anomalies of inhomogeneously textured surfaces in iterations.

References

1. L. M. Linnett, D. R. Carmichael, S. J. Clarke, Texture classification using a spatial-point process model, *IEEE Proceedings: Vision, Image and Signal Processing* 142 (1995) 1-6.

2. F. S. Cohen, Maximum likelihood unsupervised textured image segmentation, *CVGIP: Graphical Models Image Processing* 54 (1992) 239-251.

3. F. S. Cohen, Z. Fan, M. A. Patel, Classification of rotated and scaled textured images using Gaussian Markov random field models, *IEEE Transactions on Pattern Analysis and Machine Intelligence* 13 (1991) 192-202.

4. M. M. Van Hulle, T. Tollenaere, A modular artificial neural network for texture processing, Neural Networks 6 (1993) 7-32.

5. R. M. Haralick, K. Shanmugam, I. Dinstein, Textural features for image classification, *IEEE Transactions on Systems, Man and Cybernetics* 3 (1973) 610-621.

6. R. W. Conners, C. W. McMillin, K. Lin, R. E. Vasquez-Espinosa, Identifying and locating surface defects in wood, *IEEE Transactions on Pattern Analysis and Machine Intelligence* PAMI-5 (1983) 573-583.

7. L. H. Siew, R. M. Hogdson, Texture measures for carpet wear assessment, *IEEE Transactions on Pattern Analysis and Machine Intelligence* 10 (1988) 92-105.

8. K. V. Ramana, B. Ramamoorthy, Statistical methods to compare the texture features of machined surfaces, *Pattern Recognition* 29 (1996) 1447-1459.

9. S. -S. Liu, M. E. Jernigan, Texture analysis and discrimination in additive noise, *Computer Vision, Graphics and Image Processing* 49 (1990) 52-67.

10. R. Azencott, J. -P. Wang, L. Younes, Texture classification using windowed Fourier filters, *IEEE Transactions on Pattern Analysis and Machine Intelligence* 19 (1997) 148-153.

11. J. Escofet, M. S. Millan, H. Abril, E. Torrecilla, Inspection of fabric resistance to abrasion by Fourier analysis, *Proceedings of SPIE* 3490 (1998) 207-210.

12. C. -H. Chan, K. -H. Pang, Fabric defect detection by Fourier analysis, *IEEE Transactions on Industry Applications* 36 (2000) 1267-1276.

13. T. Ohshige, H. Tanaka, Y. Miyazaki, T. Kanda, H. Ichimura, N. Kosaka, T. Tomoda, Detect inspection system for patterned wafers based on the spatial-frequency filtering, *IEEE/CHMT European International Electronic Manufacturing Technology Symposium* (1991) 192-196.

14. D. -M. Tsai, C. -F. Tseng, Surface roughness classification for castings, *Pattern Recognition* 32 (1999) 389-405.

15. J. G. Daugman, Uncertainty relation for resolution in space, spatial-frequency and orientation optimized by two-dimensional visual cortical filters, *Journal of the Optical Society of America* A 2 (1985) 1160-1169.

16. M. Clark and A. C. Bovik, Texture segmentation using Gabor modulation/ demodulation, *Pattern Recognition Letters* 6 (1987) 261-267.

17. D. A. Clausi, M. E. Jernigan, Designing Gabor filters for optimal texture separability, *Pattern Recognition* 33 (2000) 1835-1849.

18. W. Polzleitner, G. Schwingskakl, Quality classification of wooden surfaces using Gabor filters and genetic feature optimization, *Proceedings of the SPIE* 3837, (1999) 220-231.

19. G. Paschos, Fast color texture recognition using chromaticity moments, *Pattern Recognition Letters* 21 (2000) 837-841.

20. K. Wiltschi, A. Pinz, T. Lindeberg, Automatic assessment scheme for steel quality inspection, *Machine Vision and Applications* 12 (2000) 113-128.

21. A. Bodnarova, M. Bennamoun, S. J. Latham, Constrained minimization approach to optimise Gabor filters for detecting flaws in woven textiles, *Proceedings of the IEEE International Conference on Acoustics, Speech and Signal Processing* 6 (2000) 3606-3609.

22. D. -M. Tsai, S. -K. Wu, Automated surface inspection using Gabor filters, *International Journal of Advanced Manufacturing Technology* 16 (2000) 474-482.

23. S. G. Mallat, A theory for multiresolution signal decomposition: the wavelet representation, *IEEE Transactions on Pattern Analysis and Machine Intelligence* 11 (1989) 674-693.

24. T. Chen, C. -C. J. Kuo, Texture analysis and classification with tree-structured wavelet transform, *IEEE Transactions on Image Processing* 2 (1993) 429-441.

25. K. Maruo, T. Shibata, T. Yamaguchi, M. Ichikawa, T. Ohmi, Automatic defect pattern detection on LSI wafers using image processing techniques, *IEICE Transactions on Electronics* E82-C (1999) 1003-1012.

26. H. Sari-Sarraf, J. S. Goddard, Jr., Robust defect segmentation in woven fabrics, *Proceedings of the IEEE Computer Society Conference on Computer Vision and Pattern Recognition* (1998) 938-944.

27. G. Lambert, F. Bock, Wavelet methods for texture defect detection, *Proceedings of the IEEE International Conference on Image Processing* 3 (1997) 201-204.

28. D. -M. Tsai and C. -Y Hsieh, Automated surface inspection for directional textures, *Image and Vision Computing* 18 (1999) 49-62.

29. D. -M. Tsai, T. -Y. Huang, Automated surface inspection for statistical textures, *Image and Vision Computing* 21 (2003) 307-323.

30. B. H. Khalaj, H. K. Aghajan, T. Kailath, Patterned wafer inspection by high resolution spectral estimation techniques, *Machine Vision and Applications* 7 (1994) 178-185.

31. P. Perona, J. Malik, Scale-space and edge detection using anisotropic diffusion, *IEEE Transactions on Pattern Analysis and Machine Intelligence*, 12 (1990), 629-639.

32. Y. -L. You, W. Xu, A. Tannenbaum, M. Kaveh, Behavioral analysis of anisotropic diffusion in image processing, *IEEE Transactions on Image Processing* 5 (1996), 1539-1553.

33. D. Barash, A fundamental relationship between bilateral filtering, adaptive smoothing, and the nonlinear diffusion equation, *IEEE Transactions on Pattern Analysis and Machine Intelligence* 24 (2002) 844-847.

34. J. Weickert, B. M. Ter, H. Romeny, M. A. Viergever, Efficient and reliable schemes for nonlinear diffusion filtering, *IEEE Transactions on Image Processing* 7 (1998) 398-410.

35. L. Alvarez, P. L. Lions, J. M. Morel, Image selective smoothing and edge detection by nonlinear diffusion, SIAM J. Numer. Anal. 29 (1992) 845-866.

36. Y. Chen, C. A. Z. Barcelos, Smoothing and edge detection by time-varying coupled nonlinear diffusion equations, *Computer Vision and Image Understanding* 82 (2001) 85-100.

37. G. Sapiro, D. L. Ringach, Anisotropic diffusion of multivalued images with applications to color filtering, *IEEE Transactions on Image Processing* 5 (1996) 1582-1586.

38. A. F. Solé, A. López, Crease enhancement diffusion, *Computer Vision and Image Understanding* 84 (2001) 241-248.

39. F. Torkamani-Azar, K. E. Tait, Image recovery using the anisotropic diffusion equation, *IEEE Transactions on Image Processing* 5 (1996) 1573-1578.

40. H. Tsuji, T. Sakatani, Y. Yashima, N. Kobayashi, A nonlinear spatio-temporal diffusion and its application to prefiltering in MPEG-4 video coding, *Proceedings of the International Conference on Image Processing I* (2002) 85-88.

41. W. J. Niessen, K. L. Vincken, J. A. Weickert, M. A. Viergever, Nonlinear multiscale representations for image segmentation, *Computer Vision and Image Understanding* 66 (1997) 233-245.

42. S. A. Bakalexis, Y. S. Boutalis, B. G. Mertzios, Edge detection and image segmentation based on nonlinear anistropic diffusion, *IEEE International Conference on Digital Signal Processing* 2 (2002) 1203-1206.

43. H. Deng, J. Liu, Unsupervised segmentation of textured images using anisotropic diffusion with annealing function, *International Symposium on Multimedia Information Processing* (2000) 62-67.

44. N. Himayat, S. A. Kassam, A theoretical study of some nonlinear edge preserving smoothing filters, *IEEE International Conference on Systems Engineering* (1991) 261-264.

45. Yongbin Zhang, Songde Ma, Unsupervised segmentation of noisy image in a multi-scale framework, *WCCC-ICSP 2000. 5th International Conference on Signal Processing Proceedings* 2 (2000) 905-909.

46. F. Thomas, A. B .Charles, S. Ken, Multiscale models for Bayesian inverse problems, *SPIE Conference on Wavelet Applications in Signal and Image Processing VII* 3813 (1999) 85-96.

47. Faguo Yang, Tianzi Jiang, Pixon-based image segmentation with Markov random fields, *IEEE Transactions on Image Processing* 12 (2003) 1552-1559.

48. K. Haris, S. N. Efstratiadis, N. Maglaveras, A. K. Katsaggelos, Hybrid image segmentation using watersheds and fast region merging, *IEEE Transactions on Image Processing* 7 (1998) 1684-1699.

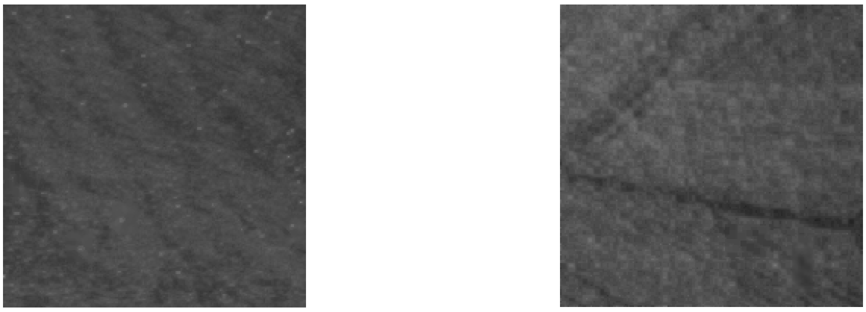

(a) (b)

Figure 1. Two sputtered surfaces of touch panels: (a) a faultless sample image; (b) a defective sample image.

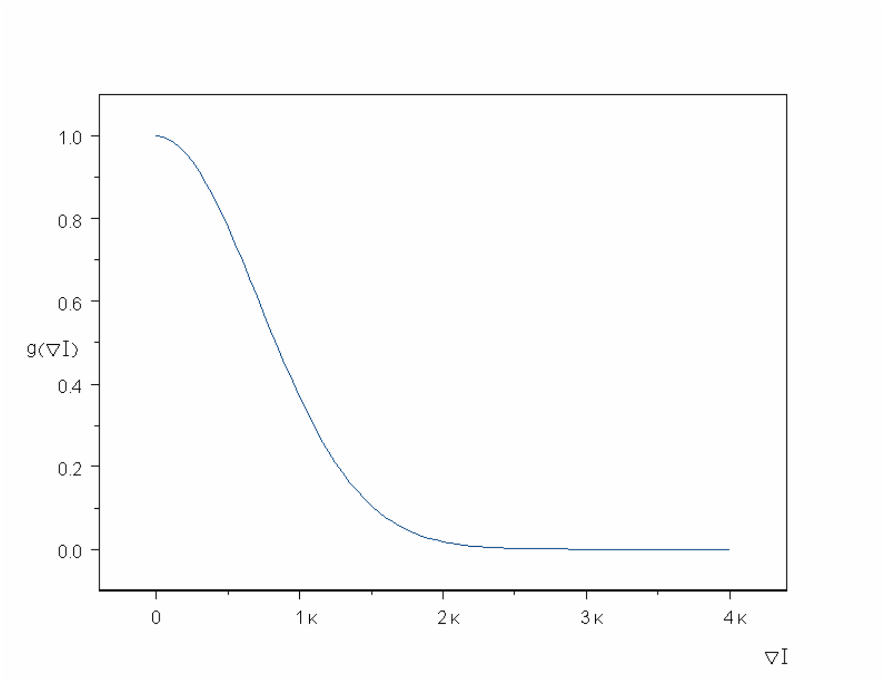

(a)

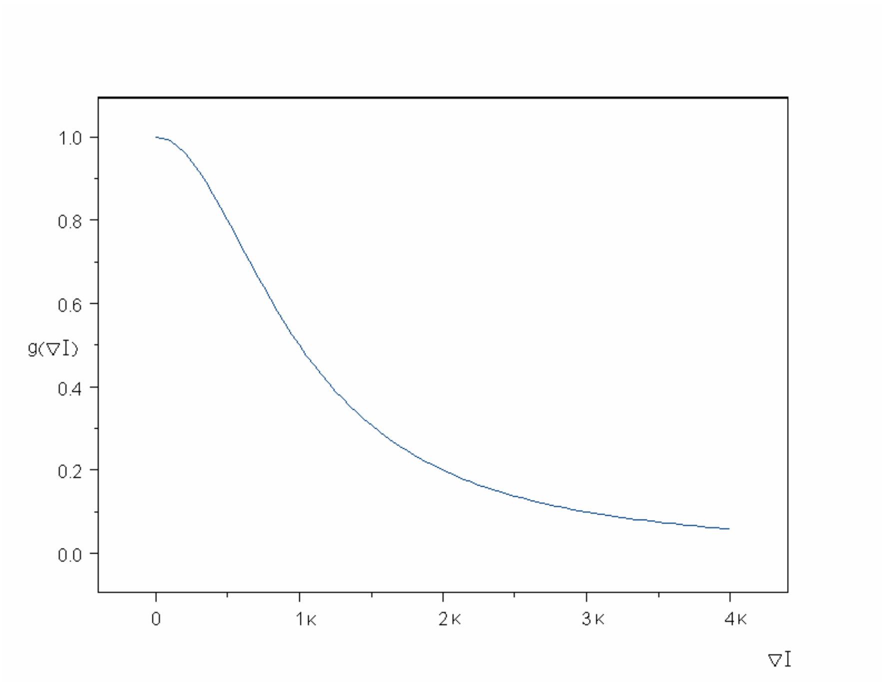

(b)

Figure 2. Graphs of two diffusion coefficient functions: (a) $g(\nabla \boldsymbol{I}) = \exp[-(|\nabla \boldsymbol{I}|/\mathcal{K})^2]$;
(b) $g(\nabla \boldsymbol{I}) = 1/[1 + (|\nabla \boldsymbol{I}|/\mathcal{K})^2]$.

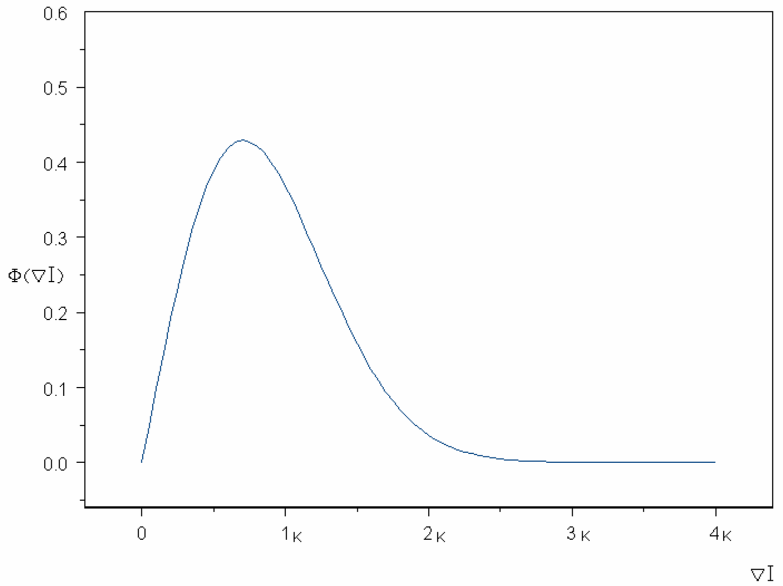

(a)

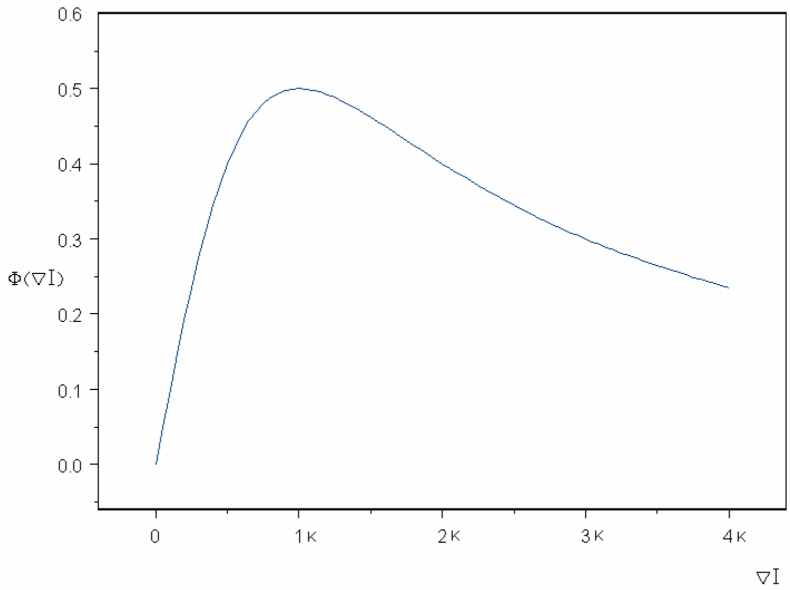

(b)

Figure 3. Graphs of two flux functions: (a) $\phi(\nabla \boldsymbol{I}) = \exp[-(|\nabla \boldsymbol{I}|/\mathcal{K})^2] \cdot \nabla \boldsymbol{I}$; (b) $\phi(\nabla \boldsymbol{I}) = \{1/[1+(|\nabla \boldsymbol{I}|/\mathcal{K})^2]\} \cdot \nabla \boldsymbol{I}$.

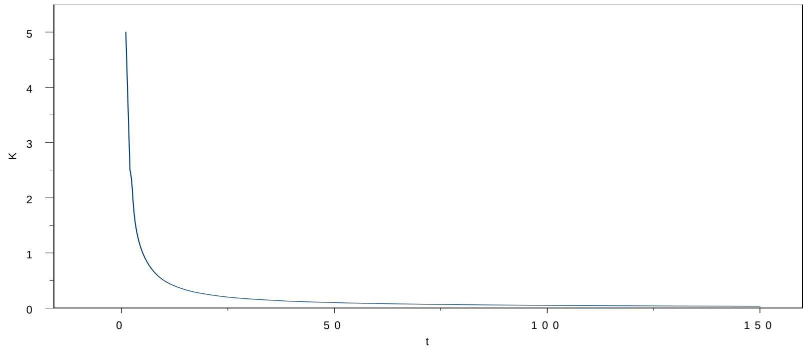

(a) n=1

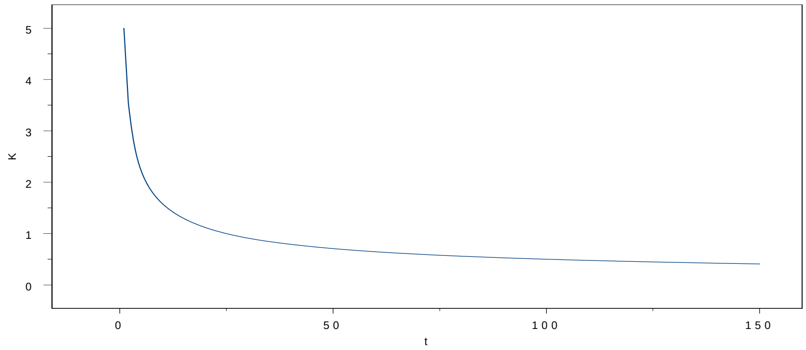

(b) n=2

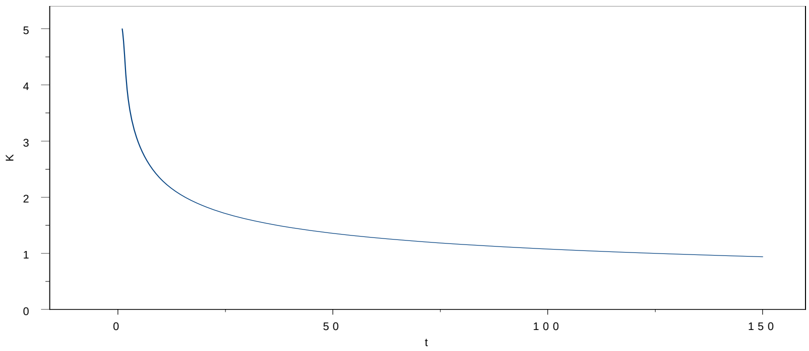

(c) n=3

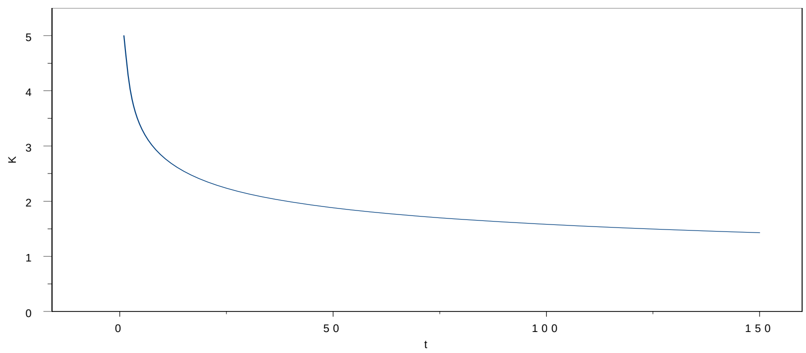

(d) n=4

Figure 4. Graphs of four root functions $\mathcal{K}(t) = \mathcal{K}(0) \cdot t^{-\frac{1}{n}}$ for n=1, 2, 3 and 4, given that $\mathcal{K}(0) = 5$.

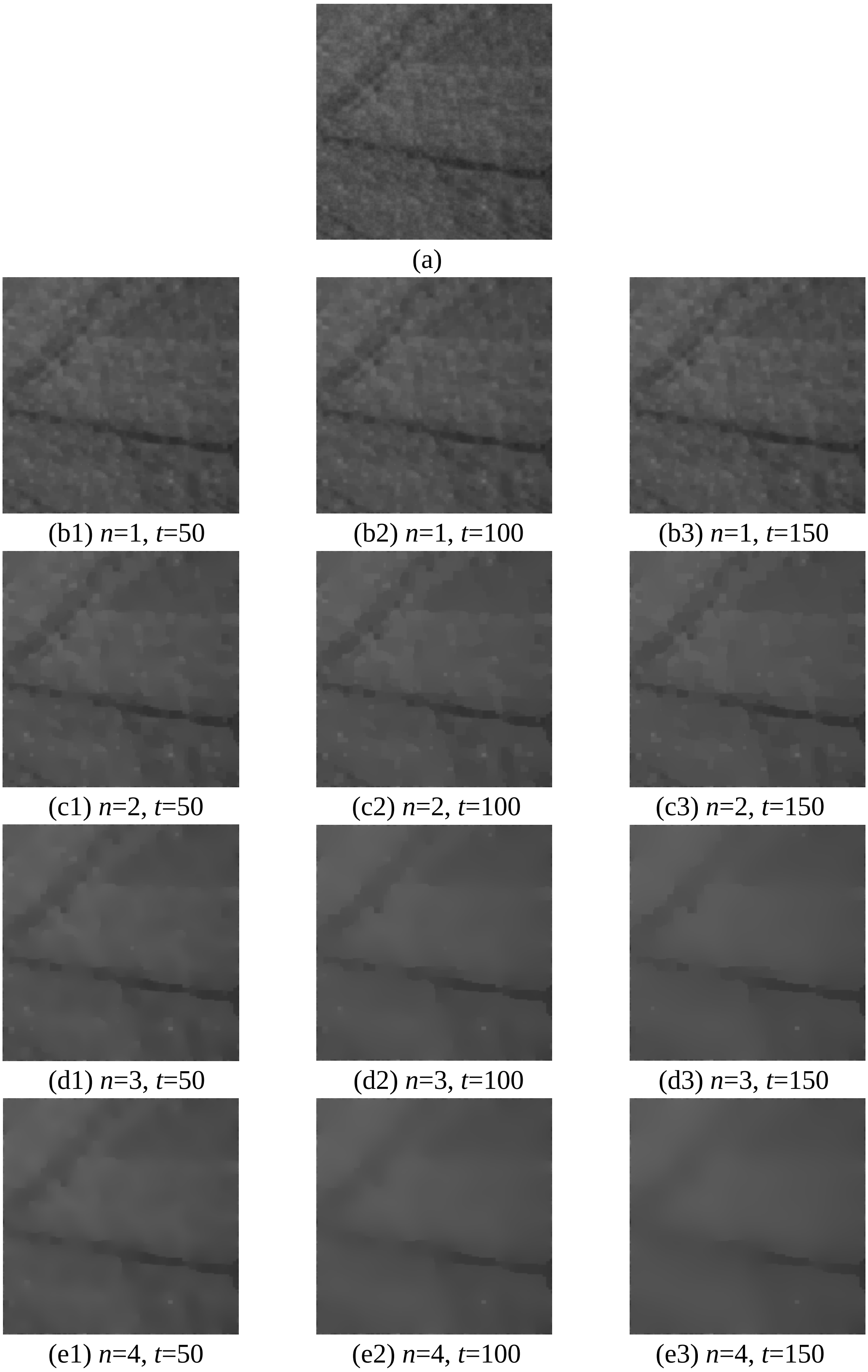

Figure 5. (a) A defective sputtered glass image; (b)-(e) the diffusion results from the four root functions $\mathcal{K}(t) = \mathcal{K}(0) \cdot t^{-\frac{1}{n}}$, n=1, 2, 3 and 4 at three iteration numbers t=50, 100 and 150, given that $\mathcal{K}(0) = 5$.

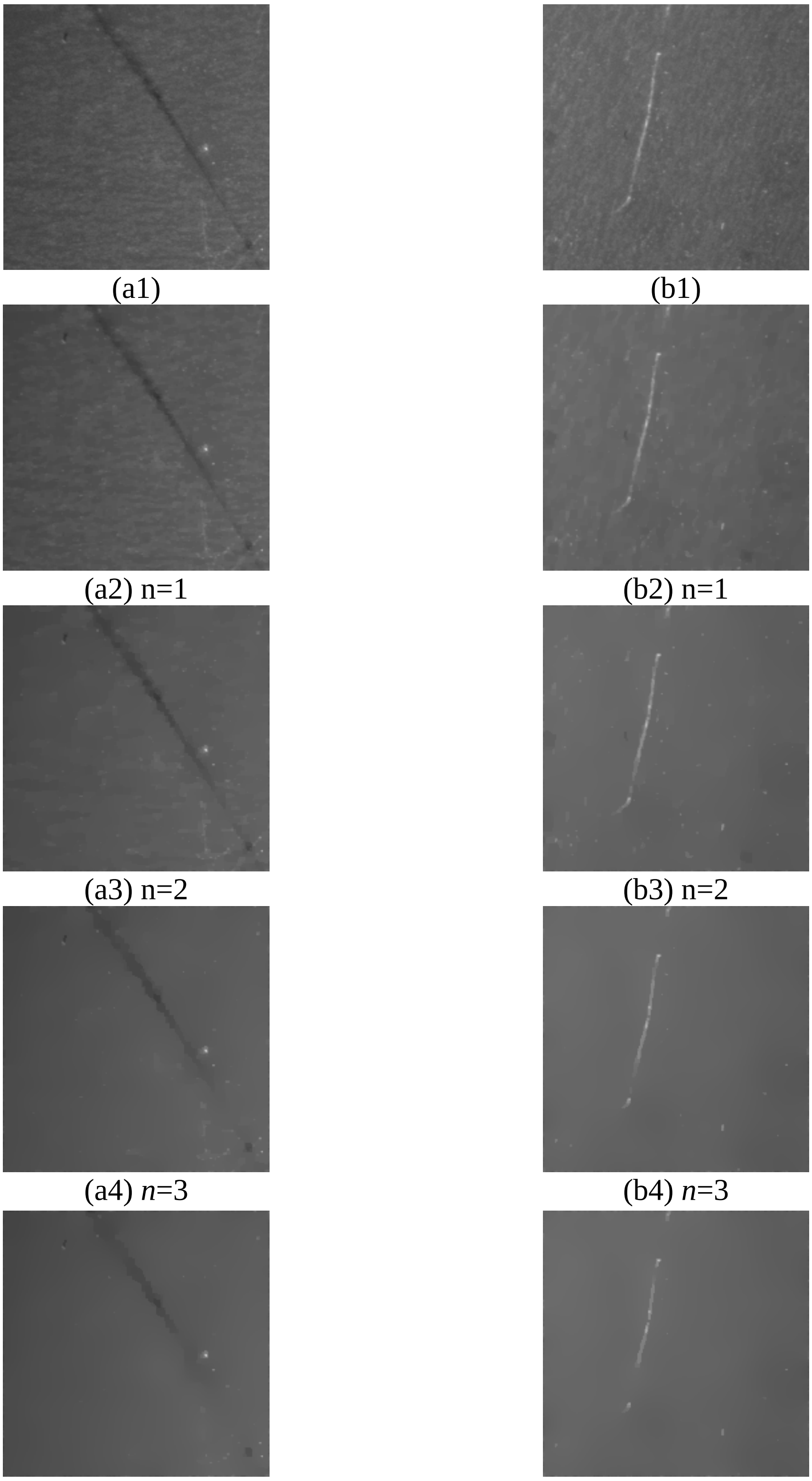

Figure 6. Two additional sample images to show the diffusion effects of different root functions: (a1)-(b1) two defective sputtered glass images; (a2)-(a5) and (b2)-(b5) the diffusion results from the four root functions $\mathcal{K}(t) = \mathcal{K}(0) \cdot t^{-\frac{1}{n}}$, n=1, 2, 3 and 4 at the iteration number t=100, given that $\mathcal{K}(0) = 5$.

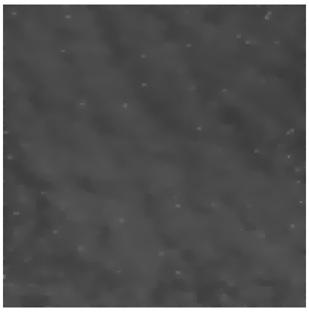

(a1) t=10

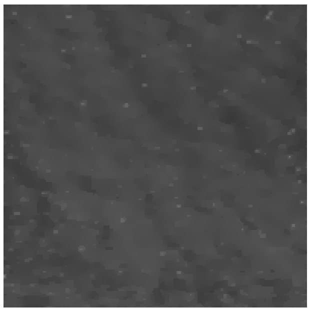

(b1) t=10

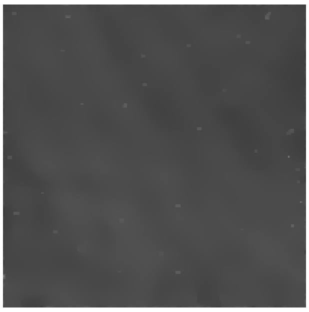

(a2) t=30

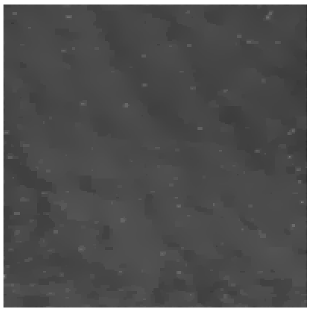

(b2) t=30

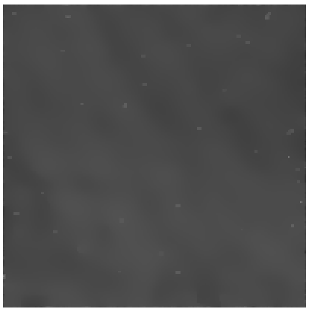

(a3) t=50

(b3) t=50

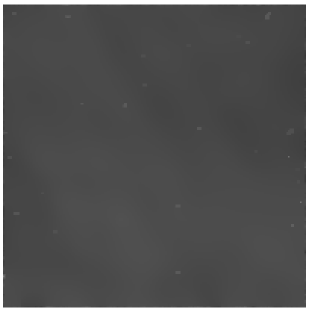

(a4) t=100

(b4) t=100

Figure 7. The diffusion results of the faultless test image in Figure 1(a) using the annealing gradient threshold $\mathcal{K}(t)$: (a1)-(a4) results from the diffusion coefficient function $g(\nabla \boldsymbol{I}) = 1/[1 + \left(|\nabla \boldsymbol{I}|/\mathcal{K}(t)\right)^2]$ at iterations t=10, 30, 50 and 100; (b1)-(b4) results from $g(\nabla \boldsymbol{I}) = \exp[-\left(|\nabla \boldsymbol{I}|/\mathcal{K}(t)\right)^2]$ at t=10, 30, 50 and 100. (Note that $\mathcal{K}(0) = 5$ is used for both functions.)

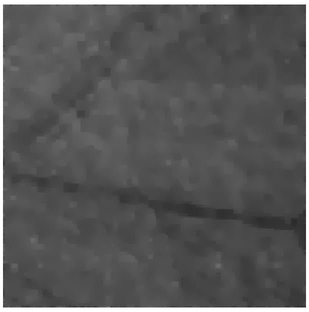

(a1) t=10

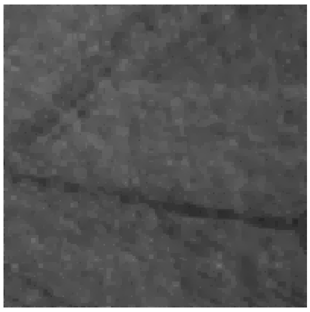

(b1) t=10

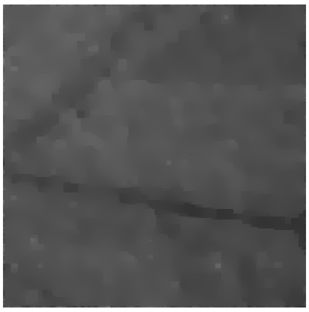

(a2) t=30

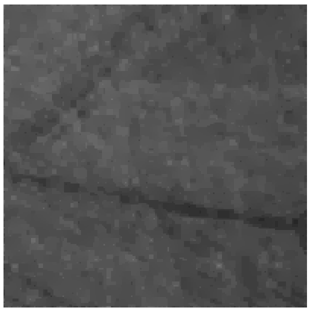

(b2) t=30

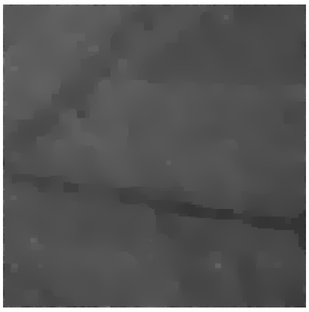

(a3) t=50

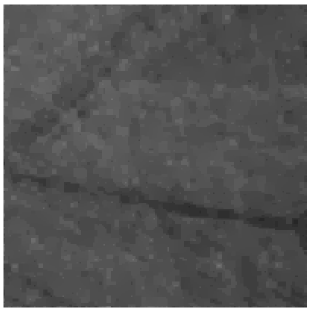

(b3) t=50

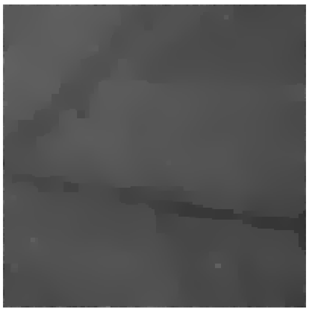

(a4) t=100

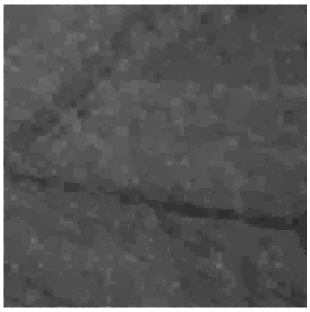

(b4) t=100

Figure 8. The diffusion results of the defective test image in Figure 1(b) using the annealing gradient threshold $\mathcal{K}(t)$: (a1)-(a4) results from the diffusion coefficient function $g(\nabla \boldsymbol{I}) = 1 \big/ [1 + \left(|\nabla \boldsymbol{I}| / \mathcal{K}(t)\right)^2]$ at iterations t=10, 30, 50 and 100; (b1)-(b4) results from $g(\nabla \boldsymbol{I}) = \exp[-\left(|\nabla \boldsymbol{I}| / \mathcal{K}(t)\right)^2]$ at t=10, 30, 50 and 100. ($\mathcal{K}(0) = 5$ is used for both functions.)

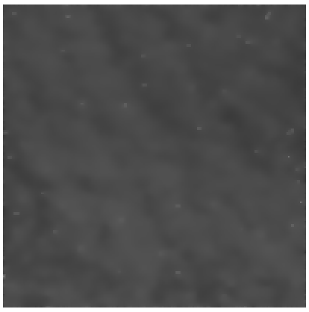

(a1) $\mathcal{K}$=5, t=10

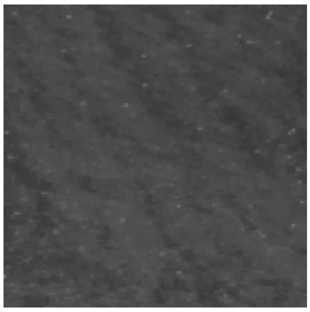

(b1) $\mathcal{K}$=1, t=10

(a2) $\mathcal{K}$=5, t=30

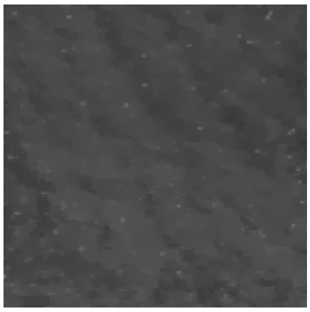

(b2) $\mathcal{K}$=1, t=30

(a3) $\mathcal{K}$=5, t=50

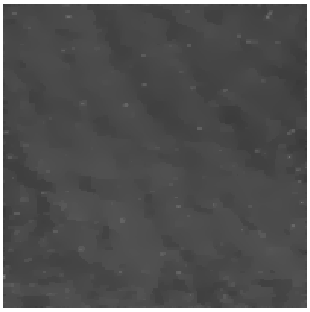

(b3) $\mathcal{K}$=1, t=50

(a4) $\mathcal{K}$=5, t=100

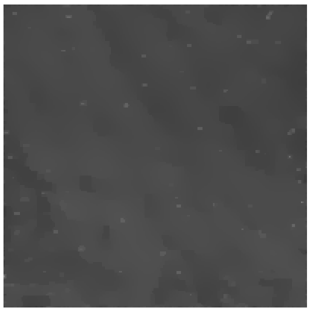

(b4) $\mathcal{K}$=1, t=100

Figure 9. The diffusion results of the faultless test image in Figure 1(a) using a constant $\mathcal{K}$: (a1)-(a4) results from a large $\mathcal{K}$ value of 5 at iterations t=10, 30, 50 and 100; (b1)-(b4) results from a small $\mathcal{K}$ value of 1 at iterations t=10, 30, 50 and 100. (Note that the diffusion coefficient function $g(\nabla \boldsymbol{I}) = 1/[1 + (|\nabla \boldsymbol{I}|/\mathcal{K})^2]$ is used, where $\mathcal{K} = 5$ or $\mathcal{K} = 1$ is applied for all iterations.)

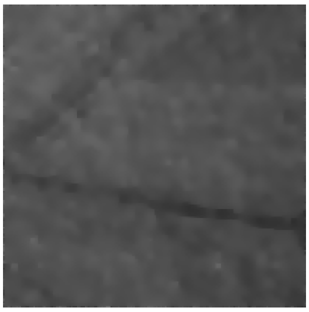

(a1) $\mathcal{K}$ =5, t=10

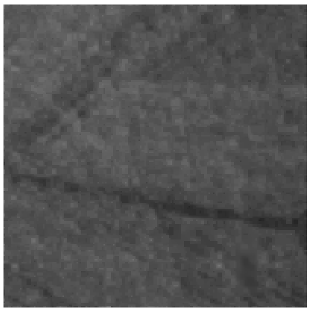

(b1) $\mathcal{K}$ =1, t=10

(a2) $\mathcal{K}$ =5, t=30

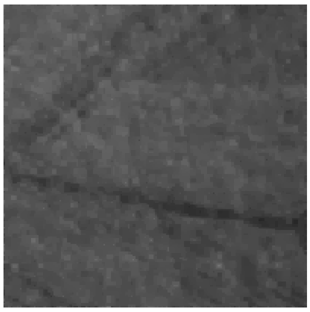

(b2) $\mathcal{K}$ =1, t=30

(a3) $\mathcal{K}$ =5, t=50

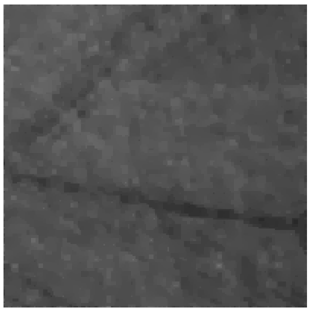

(b3) $\mathcal{K}$ =1, t=50

(a4) $\mathcal{K}$ =5, t=100

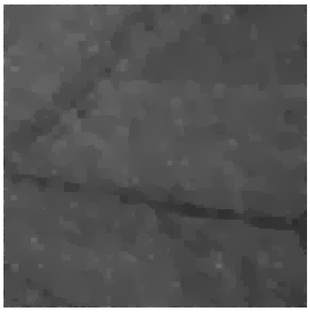

(b4) $\mathcal{K}$ =1, t=100

Figure 10. The diffusion results of the defective test image in Figure 1(b) using a constant $\mathcal{K}$: (a1)-(a4) results from a large $\mathcal{K}$ value of 5 at iterations t=10, 30, 50 and 100; (b1)-(b4) results from a small $\mathcal{K}$ value of 1 at iterations t=10, 30, 50 and 100. (Note that the diffusion coefficient function $g(\nabla \boldsymbol{I}) = 1 / [1 + (|\nabla \boldsymbol{I}| / \mathcal{K})^2]$ is used, where $\mathcal{K} = 5$ or $\mathcal{K} = 1$ is applied for all iterations.)

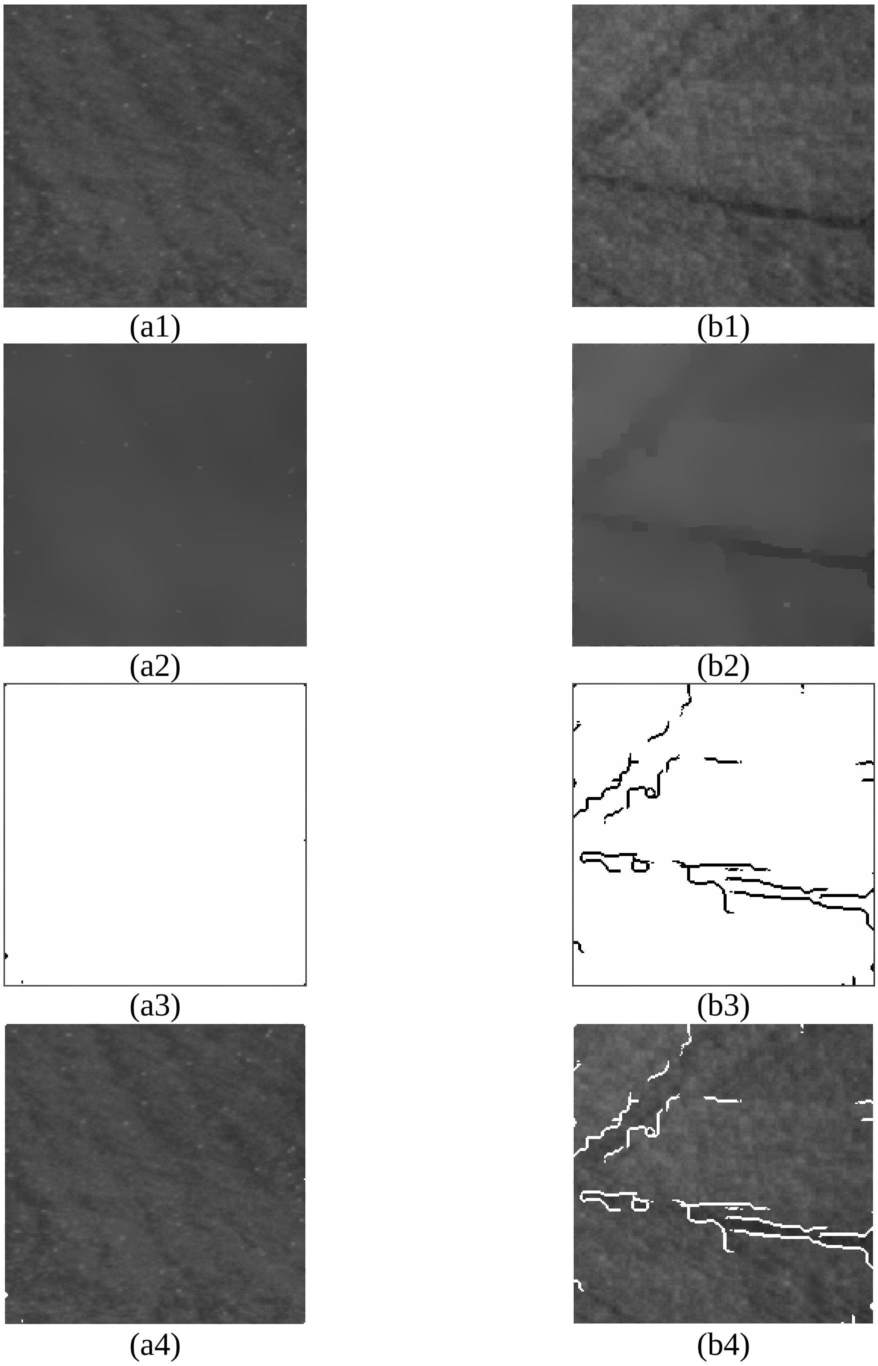

Figure 11. Detecting edges of defect regions in the final diffused images: (a1)-(b1) a faultless and a defective sputtered glass surface images; (a2)-(b2) respective diffusion results at iteration number 150 with $\mathcal{K}(0) = 5$; (a3)-(b3) the detected edges shown as binary images; (a4)-(b4) the results of superimposing the detected edges on the original images.

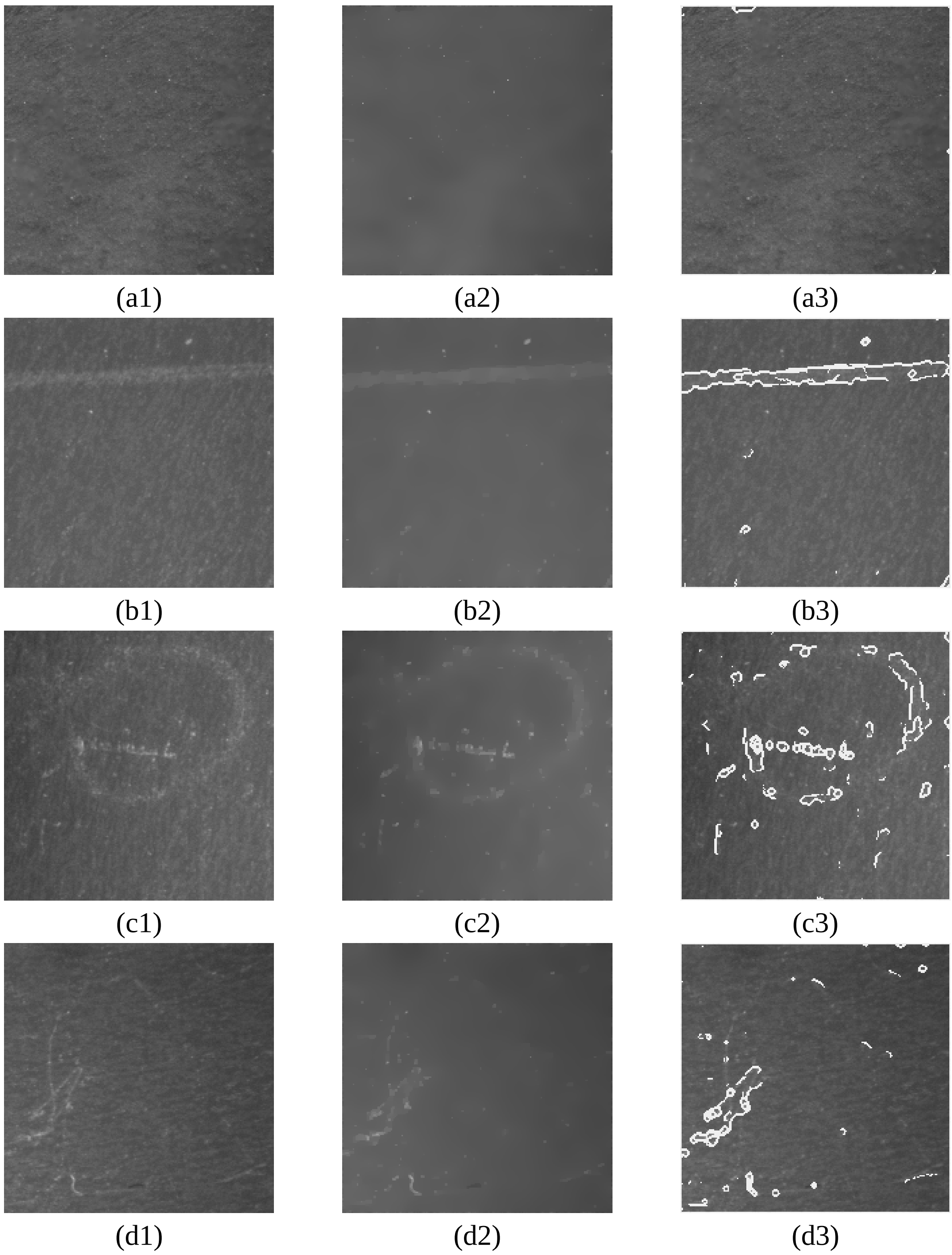

Figure 12. The diffusion results for sputtered glass surfaces under a high image resolution: (a1)-(h1) a faultless and seven defective test images; (a2)-(h2) the respective diffusion results at iteration t=50 from the diffusion coefficient function of eq. (7) with $\mathcal{K}(0)=4$ for all samples; (a3)-(h3) the superimposing results of detected edges of defect regions.

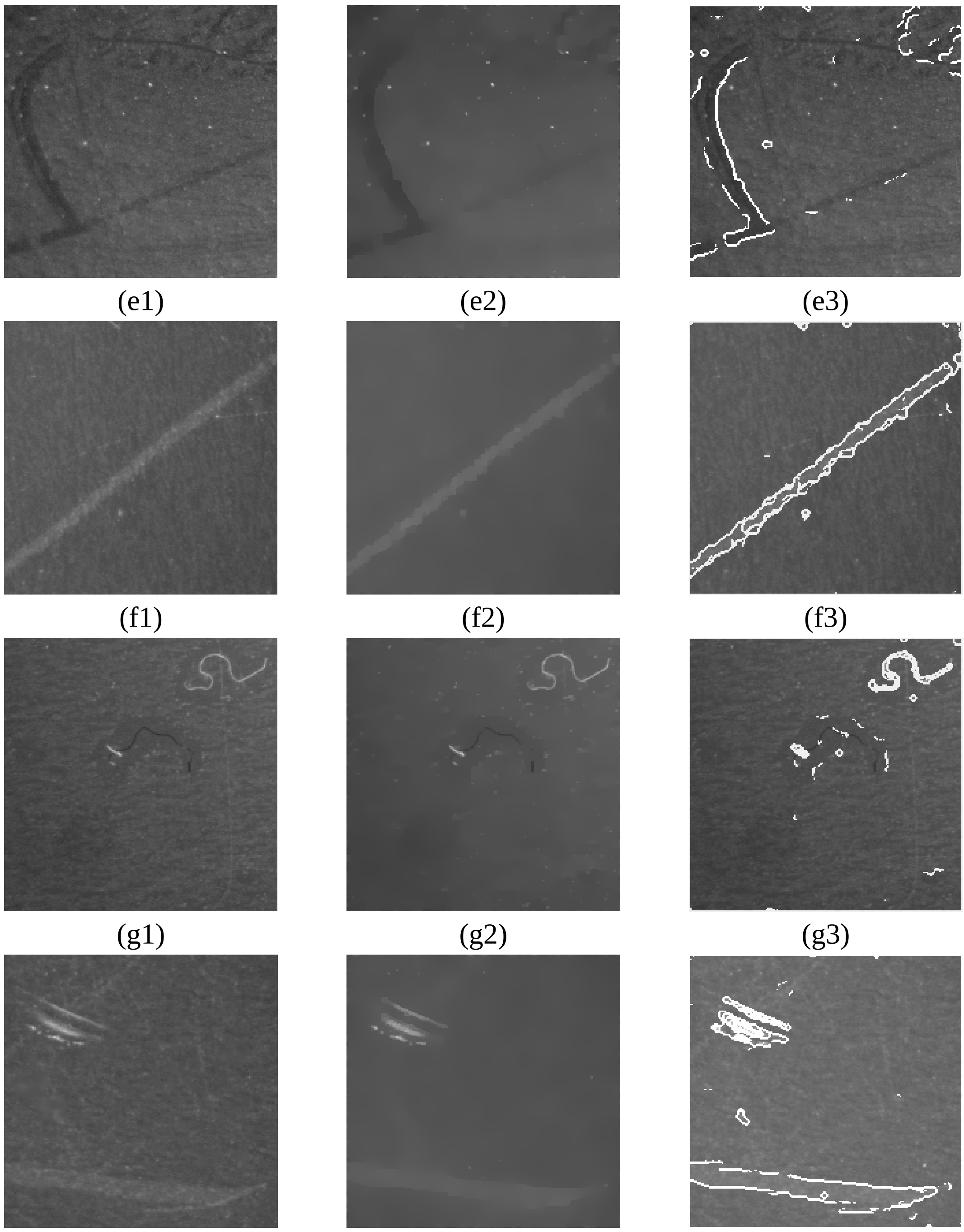

Figure 12. (continued)

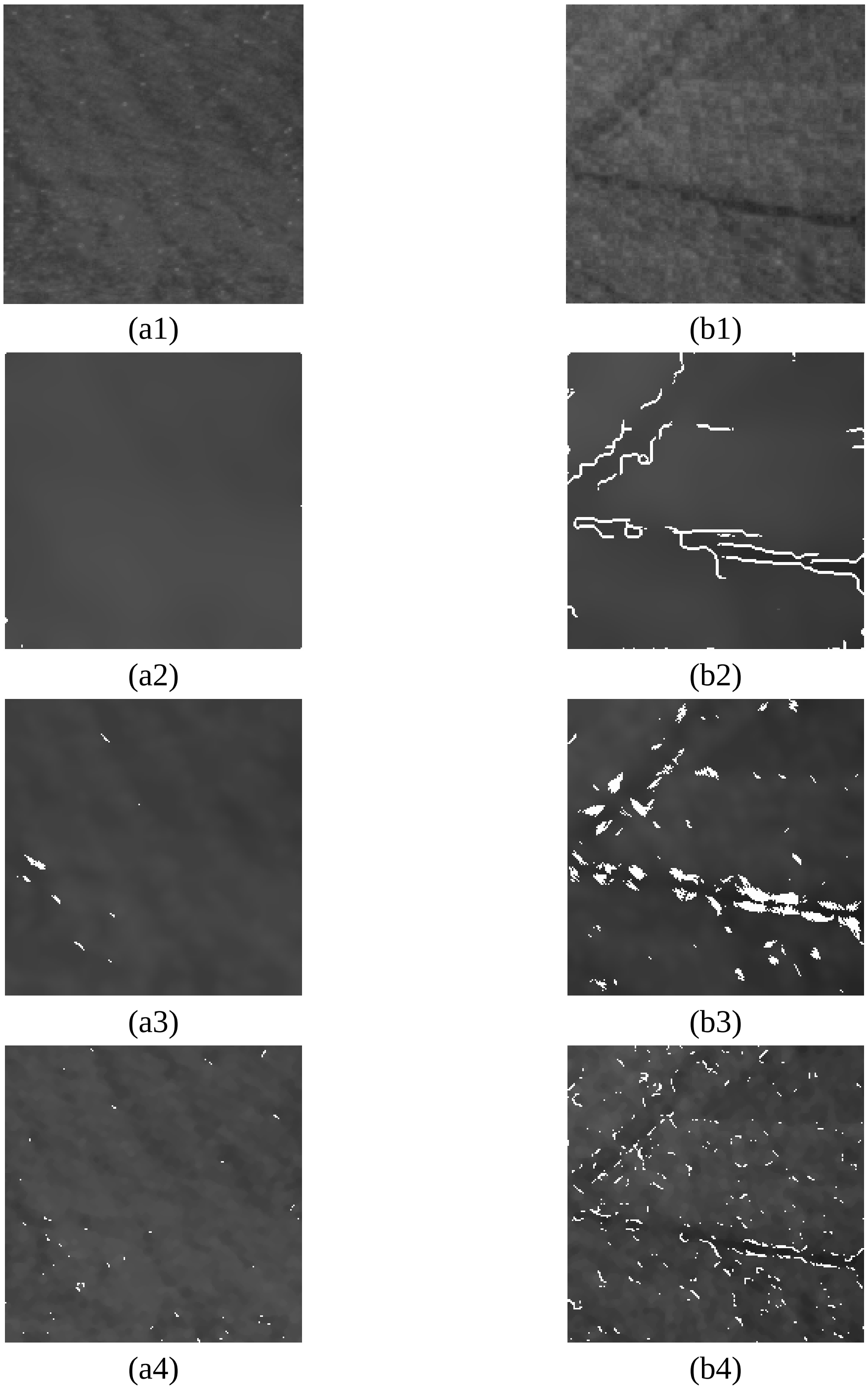

Figure 13. Comparison of various filtering methods for test samples I: (a1) the original image of a clear surface; (b1) the original image of a defective surface; (a2)-(b2) detection results of superimposing the thresholded edges on the filtered images from the proposed diffusion method; (a3)-(b3) detection results from the Gaussian filtering; (a4)-(b4) detection results from the median filtering.

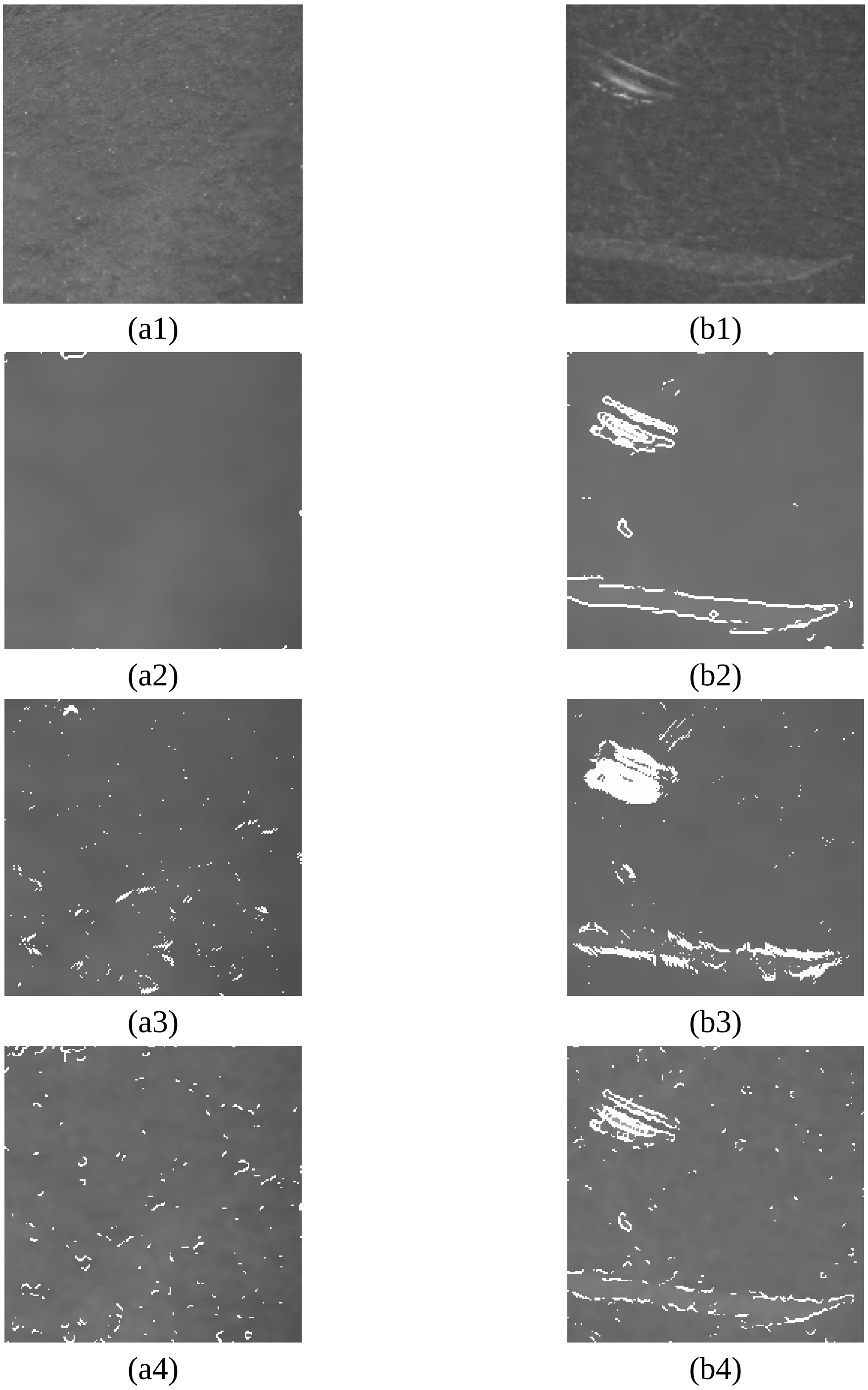

Figure 14. Comparison of various filtering methods for test samples II: (a1) the original image of a clear surface; (b1) the original image of a defective surface; (a2)-(b2) detection results from the proposed diffusion method; (a3)-(b3) detection results from the Gaussian filtering; (a4)-(b4) detection results from the median filtering.